New Deep-Blue-Emitting Ce-Doped $A_{4-m}B_nC_{19+2m-n}X_{29+m}$ (A = Sr, La; B = Li; C = Si, Al; X = O, N; 0 ≤ m ≤ 1; 0 ≤ n ≤ 1) Phosphors for High-Color-Rendering Warm White Light-Emitting Diodes

Wang, Chun Yun; Takeda, Takashi; Melvin Ten Kate, Otmar; Funahashi, Shiro; Xie, Rong Jun; Takahashi, Kohsei; Hirosaki, Naoto

DOI
10.1021/acsami.9b09982

Publication date
2019

Document Version
Final published version

Published in
ACS Applied Materials and Interfaces

ACS APPLIED MATERIALS & INTERFACES

Research Article

Cite This: ACS Appl. Mater. Interfaces 2019, 11, 29047−29055

www.acsami.org

New Deep-Blue-Emitting Ce-Doped $A_{4-m}B_nC_{19+2m}X_{29+m}$ (A = Sr, La; B = Li; C = Si, Al; X = O, N; $0 \le m \le 1$; $0 \le n \le 1$) Phosphors for High-Color-Rendering Warm White Light-Emitting Diodes

Chun-Yun Wang,[*,†,‡,§] Takashi Takeda,[*,†,‡] Otmar Melvin ten Kate,[†,∥] Shiro Funahashi,[†] Rong-Jun Xie,[⊥] Kohsei Takahashi,[†] and Naoto Hirosaki[†]

[†]Sialon Group, National Institute for Materials Science, Namiki 1-1, Tsukuba, Ibaraki 305-0044, Japan

[‡]Graduate School of Chemical Sciences and Engineering, Hokkaido University, Sapporo, Hokkaido 060-6828, Japan

[§]Tsinghua-Berkeley Shenzhen Institute, Tsinghua University, Shenzhen 51800, China

[∥]Department of Chemical Engineering, Applied Sciences, Delft University of Technology, Delft 2629HZ, Netherlands

[⊥]College of Materials, Xiamen University, Simingnan-Road 422, Xiamen 361005, P. R. China

Supporting Information

ABSTRACT: A new sialon $Eu_{3.60}LiSi_{13.78}Al_{6.03}O_{6.82}N_{22.59}$ has been discovered via the single-particle diagnosis approach. Its crystal structure (space group $P3m1$) was solved and refined from single-crystal X-ray diffraction data. It has the interesting feature of two types of disorder at the Eu2 site: positional disorder (Eu2a/Eu2b) and substitutional disorder with $(Si/Al)_2(O/N)$. The structure is generalized to the formula $A_{4-m}B_nC_{19+2m}X_{29+m}$ (A = Sr, La, Eu, Ce; B = Li; C = Si, Al; X = O, N; $0 \le m \le 1$; $0 \le n \le 1$), of which $Sr_{3.61}LiSi_{14.27}Al_{5.61}O_{6.19}N_{23.25}$ (Sr−sialon, $m = 0.41$, $n = 1$) and $La_{2.85}Sr_{0.76}LiSi_{14.86}Al_{4.93}O_{2.89}N_{26.51}$ (LaSr-sialon, $m = 0.40$, $n = 1$) are two examples that have been obtained as a single-phase powder. Sr-sialon:Eu and LaSr-sialon:Eu both show blue to yellow emission, depending on the Eu concentration, whereas Sr-sialon:1% Ce shows a deep-blue emission band centered at 422 nm with a full width at half-maximum of 80 nm and an internal quantum efficiency of 80% (λ_{ex} = 355 nm). The latter phosphor has very good thermal stability of both emission intensity and color. A white light-emitting diode (LED) containing the newly discovered Sr-sialon:5% Ce as the blue phosphor component shows excellent color-rendering indices (R_a = 96 and R_{12} = 97) with a correlated color temperature of 4255 K. This indicates that Sr-sialon:Ce is a highly promising deep-blue phosphor for illumination grade white LEDs.

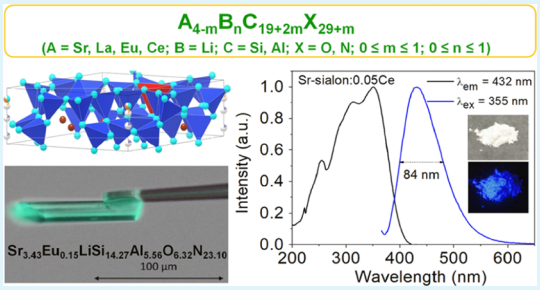

KEYWORDS: *single-particle diagnosis approach, new sialon phosphors, deep-blue-emitting, high-color-rendering, warm white LEDs*

1. INTRODUCTION

M−Si−Al−O−N (sialon) materials, where M is usually an alkaline earth or rare earth element, have been extensively investigated as ceramics for several decades because of their excellent high-temperature mechanical properties and thermal shock resistance.[1,2] The good chemical and thermal stability and high structural flexibility make sialons hot candidates as host materials for white light-emitting diode (LED) phosphors. Several oxynitride phosphors that developed from sialon phase materials turned out to have good photoluminescence properties, promising for phosphor-converted white LED (pc-wLED) application. The examples are β-sialon:Eu ($Si_{6-z}Al_zO_zN_{8-z}$:Eu),[3] Ca-α-sialon:Ce ($Ca_{m/2}Si_{12-(m+n)}Al_{m+n}O_nN_{16-n}$:Ce),[4] $La_3Si_{6.5}Al_{1.5}N_{9.5}O_{5.5}$:$Ce^{3+}$,[5] $Sr_5Al_{5+x}Si_{21-x}N_{35-x}O_{2+x}$:$Eu^{2+}$ ($x \approx 0$),[6] $MAl_{2-x}Si_xO_{4-x}N_x$:Eu^{2+} (M = Ca, Sr, Ba),[7] $Gd_3Al_{3+x}Si_{3-x}O_{12+x}N_{2-x}$:$Ce^{3+}$,[8] $BaSi_3Al_3O_4N_5$:Eu,[9] and LaAl$(Si_{6-z}Al_z)(N_{10-z}O_z)$:$Ce^{3+}$.[10]

There are two main ways in order to obtain efficient phosphor-converted white LEDs: (1) a blue LED chip in combination with a mixture of red and green phosphors, and (2) a UV/near-UV LED chip with a mixture of red, green, and blue phosphors. However, to obtain a high-power white LED with very high color stability, a UV excitable white LED is preferred over a blue excitable LED. A UV-excitable LED has better color stability as its color is solely determined by the emission light of the phosphors.[11] Furthermore, for high-power white LEDs, a UV LED chip has the advantage over a blue LED chip in that it has less current drooping and less binning at high current.[12] The blue phosphor that needs to be used in such a UV LED chip should preferably have a peak emission wavelength in the 410−450 nm range, as a phosphor with a shorter wavelength will have a part of its emission in the spectral range for which the human eye is not sensitive enough,

Received: June 7, 2019
Accepted: July 11, 2019
Published: July 11, 2019

DOI: 10.1021/acsami.9b09982
ACS Appl. Mater. Interfaces 2019, 11, 29047−29055

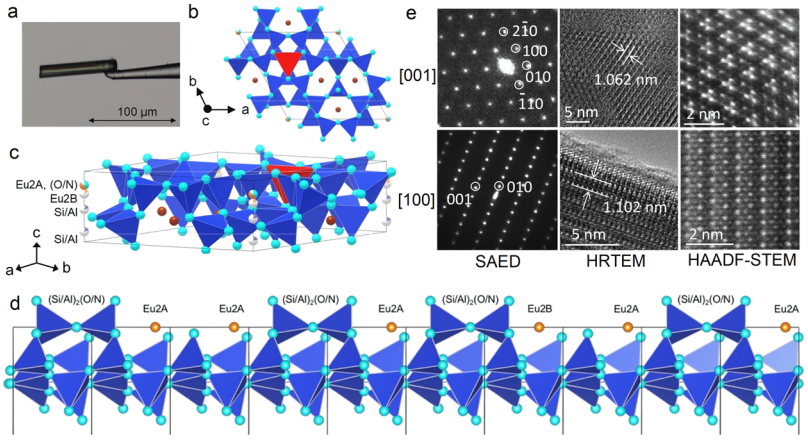

Figure 1. (a) Photograph of the selected columnar crystal; Crystal structure of $Eu_{3.60}LiSi_{13.78}Al_{6.03}O_{6.82}N_{22.59}$ (b) from the [001] direction and (c) from the [111] direction. Blue and red tetrahedra are $(Si/Al)(O/N)_4$ and $Li(O/N)_4$, respectively. Brown spheres are Eu (Eu1), light blue spheres are (O/N). The substitutional disorder part on the (0, 0, z) axis is shown by three possible parts (Eu2A, Eu2B, and $(Si/Al)_2(O/N)$). The color-divided balls represent the site occupancies. These images were drawn with the program VESTA.[31] (d) Schematic representation of the disorder part of $Eu_{3.60}LiSi_{13.78}Al_{6.03}O_{6.82}N_{22.59}$. The fraction of Eu2A, Eu2B, and $(Si/Al)_2(O/N)$ is based on the refined value. (e) SAED patterns, HRTEM, and HAADF-STEM images from the [001] (above) and [100] (below) zone axis.

whereas a phosphor with a longer wavelength is not blue enough, lowering the color-rendering index.[13,14]

However, although several efficient green-, yellow-, and red-emitting sialon phosphors have been developed and even commercially applied, there is still a lack of highly efficient and thermally stable deep-blue emission phosphors. Only a few (oxy-)nitride phosphors have been reported of which the emission is in the 410−450 nm region. $LaSiO_2N$:Ce and $YSiO_2N$:Ce have their emission peaks at 415−430 nm and at 430−450 nm respectively, but both compounds have a low luminescence efficiency and a fast thermal quenching.[15,16] A similar low quantum efficiency and fast thermal quenching is also seen for $Gd_5Si_3O_{12}N$:Ce with an emission maximum at 427−437 nm.[17] $LaSi_3N_5$:Ce with an emission maximum between 424 and 444 nm shows a relatively high-luminescence efficiency at 355 nm excitation, especially after heat treatment of the phosphor.[18] However, thermal quenching reduces the emission intensity by almost 50% at 250 °C.[18] Recently, we reported the deep-blue emission by $La_3Si_{6.5}Al_{1.5}N_{9.5}O_{5.5}$:Ce, showing an efficient (IQE = 84%) emission with a maximum at 418 nm, but also for this phosphor the thermal quenching is still considerable.[5] The deep-blue-emitting $LaAl(Si_{6-z}Al_z)(N_{10-z}O_z)$:Ce with 430 nm emission is more thermally stable, but it has a slightly lower efficiency (IQE = 75%).[10] Other blue-emitting phosphors, which have high quantum efficiency and are thermally stable, have been reported, such as AlN:Eu[19] and $BaSi_3Al_3O_4N_5$:Eu^{2+},[9] However, their emission peaks are at longer wavelengths > 450 nm.

In order to discover new phosphors, several methods have been developed,[20] such as mineral-inspired prototype evolution and new phase construction,[21] heuristics-assisted combinatorial chemistry,[22] and the single-particle diagnosis approach.[23,24] The latter allows for a fast and simple way to discover new phosphors without the need to grow large-size single crystals. New phosphors are discovered by analyzing candidate particles from mixture products synthesized by a conventional powder process with single-crystal X-ray diffraction (XRD) and microspectroscopy. With this approach, several types of nitride and oxynitride phosphors have been discovered, such as $Sr_2B_{2-2x}Si_{2+3x}Al_{2-x}N_{8+x}$:Eu,[25] $Ba_2LiSi_7AlN_{12}$:Eu,[26] and $Sr_3Si_{8-x}Al_xO_{7+x}N_{8-x}$:Eu.[27]

In this work, a new series of sialon phase $A_{4-m}B_nC_{19+2m}X_{29+m}$ (A = Sr, La, Eu, Ce; B = Li; C = Si, Al; X = O, N; $0 \le m \le 1$; $0 \le n \le 1$) is reported, discovered by the single-particle-diagnosis approach. The crystal structure and photoluminescence properties induced by Eu or Ce doping, including thermal quenching, quantum efficiency, and luminescence decay, of these new phosphors are investigated, as well as the application in a white LED.

2. MATERIALS AND METHODS

2.1. Synthesis. The starting materials of Si_3N_4 (Ube, E10), AlN (Tokuyama, E-grade), Li_3N (Kojundo Chemical, 2 N), and Eu_2O_3 (Shin-etsu Chemical, 3 N) were mixed in a glove box filled with nitrogen. The mixture was filled in a boron nitride crucible and fired in a nitrogen atmosphere of 0.92 MPa at 1900 °C for 2 h. The products were used for single-crystal pick-up.

Nondoped and Eu- or Ce-doped $A_{4-m}B_nC_{19+2m}X_{29+m}$ (A = Sr, La; B = Li; C = Si, Al; X = O, N; $0 \le m \le 1$; $0 \le n \le 1$) powders have been prepared by solid-state reaction synthesis. The starting materials (EuN, Sr_3N_2, LaN, Li_3N, Si_3N_4, SiO_2, AlN and CeN) were mixed in a glove box filled with nitrogen by following the designed chemical compositions, and then packed in a boron nitride crucible for firing. The samples were sintered in a gas pressure furnace at 0.92 MPa for 2 h at a temperature of 1850 °C. After synthesis, the samples were crushed to powder and fired again for 2 h at the same temperature. The final products were finely ground for further characterization.

2.2. X-ray Diffraction. The products were irradiated by a 370 nm UV LED lamp, and luminescent particles were selected under microscopic observation. The selected particles were mounted at the top of a glass capillary with glue, and the single crystal XRD data of the single particle were collected using a diffractometer (Bruker-AXS, SMART APEX II Ultra) with Mo Kα radiation (λ = 0.71073 Å) and multilayer focusing mirrors as a monochromator operated at 50 kV and 50 mA. The absorption corrections were applied using the multiscan procedure SADABS.[28] The crystal structure was solved by direct methods implemented in SHELXL-97.[29] Refinement of the crystal structure was carried out with anisotropic displacement parameters for all atoms by full-matrix least-squares calculation on F^2 in SHELXL-2013.[29] The elemental analysis was conducted using a scanning electron microscope (Hitachi High-Technology, SU1510) equipped with an energy-dispersive spectroscopy instrument (Bruker AXS, XFlash SDD) operated at 15 kV. The powder XRD was measured by Rigaku SmartLab with Cu Kα1 radiation (λ = 1.54056 Å) under 40 kV and 200 mA.

DOI: 10.1021/acsami.9b09982
ACS Appl. Mater. Interfaces 2019, 11, 29047−29055

2.3. Electron Microscopy. For transmission electron microscopy (TEM) observation, the finely crushed $Eu_{3.60}LiSi_{13.78}Al_{6.03}O_{6.82}N_{22.59}$ powder was dispersed in absolute ethanol and dropped on copper finder grids. The grids then were fixed on double-tilt holders. The high-resolution TEM (HRTEM), selected area electron diffraction (SAED), and scanning TEM using a high-angle annular dark-field (STEM-HAADF) detector were performed using a JEM-ARM200F (JEOL) at 200 kV. Digital micrograph software was used for analysis of the HRTEM and SAED images.

2.4. Luminescence Measurements. The photoluminescence spectra at room temperature were measured with a spectrophotometer (Hitachi F-4500) equipped with a 150 W Xe lamp. The 2D photoluminescence spectra were recorded with a FP-8600 fluorescence spectrometer (JASCO). The diffuse reflectance spectra were measured with a UV/vis spectrophotometer (JASCO V-570). The temperature-dependent emission spectra for the low-temperature (4−298 K) and high-temperature range (298−573 K) were obtained using an MCPD-9800 and an MCPD-7000 spectrometer (Otsuka Electronics), respectively. A He cryostat was used for cooling down the sample. The MCPD-9800 spectrometer, in combination with an integrating sphere, was also used to measure the reflectance and emission of the phosphors, from which the internal quantum efficiency (IQE) was calculated, as described in our previous work.[30] The luminescence decay curves were obtained with a time-correlated single photon counting system (HORIBA), excited with a 370 nm nanoLED with 1.2 ns pulse duration.

A white LED was fabricated by combining a UV LED chip (365 nm) with commercial green- ($SrSi_2O_2N_2:Eu^{2+}$) and red-emitting ($(Sr_{0.9}Ca_{0.1})AlSiN_3:Eu^{2+}$) phosphors and the prepared 5% Ce-doped $Sr_{3.61}LiSi_{14.27}Al_{5.61}O_{6.19}N_{23.25}$ (Sr-sialon) blue phosphor. The white LED was operated at a bias current of 20 mA and a voltage of 3.7 V. The electroluminescence spectrum was collected with an IMS5000 spectrometer (Asahi Spectra, Japan).

3. RESULTS AND DISCUSSION

3.1. Discovery of the $A_{4-m}B_nC_{19+2m}X_{29+m}$ (A = Sr, La, Eu, Ce; B = Li; C = Si, Al; X = O, N; $0 \le m \le 1$; $0 \le n \le 1$) Phase and its Crystal Structure. A variety of Eu/Li/Si/Al cation compositions were investigated and a new crystal was identified from a composition of Eu/Li/Si/Al = 0.05:3:11:4. The crystal was formed as a columnar shape with dimensions of 94 μm × 12 μm × 12 μm as shown in Figure 1a. With the refinement of the single-crystal XRD data, the crystal structure of the new crystal was solved and it has a trigonal unit cell of a = 12.12130(11) Å and c = 4.89283(5) Å with the $P3m1$ space group (no. 156). The crystallographic data, the atomic coordinates, and isotropic displacement parameters are shown in Tables 1 and 2, respectively. EDS was used for Al/Si ratio analyses, whereas the O/N ratio was determined from charge neutrality of the total chemical composition. The composition was determined to be $Eu_{3.60}LiSi_{13.78}Al_{6.03}O_{6.82}N_{22.59}$. The crystal structure that was finally obtained is depicted in Figure 1b. Si/Al occupies the tetrahedral sites (blue tetrahedron) and Li occupies the independent tetrahedral site (red tetrahedron). These tetrahedra form a three-dimensional framework by corner-sharing. There are two Eu sites. The Eu1 site (brown ball) is on the one-dimensional channel along the c direction and coordinated by nine O/N atoms. Another Eu (Eu2 site) is on the (0, 0, z). The early refinement resulted in the large anisotropic displacement parameter U[33] and a positional disorder at the Eu2 site was therefore expected. The splitting atom model (Eu2A/Eu2B) was used to represent the disorder of the Eu2 site. The refined separation distance between Eu2A and Eu2B is 0.62 Å. $Eu_{3.60}LiSi_{13.78}Al_{6.03}O_{6.82}N_{22.59}$ also contains a substitutional disorder on the same (0, 0, z) axis described by the alternative occupation of Eu2 (Eu2A, Eu2B) or $(Si/Al)_2(O/N)$. The fraction of Eu2A, Eu2B, and $(Si/Al)_2(O/N)$ is 0.46:0.14:0.40, respectively. In Figure 1c, Eu2A, Eu2B, and $(Si/Al)_2(O/N)$ are shown together and the color-divided balls represent the site occupancies. The O/N position of $(Si/Al)_2(O/N)$ is the same as the Eu2A site and the ball is divided by three colors (Eu2A/O/N: vacancy = 0.46:0.40:0.14). Eu2A and Eu2B are coordinated by six and nine O/N atoms, respectively. The example of the crystal structure estimated from the fraction of Eu2A, Eu2B, and $(Si/Al)_2(O/N)$ is depicted in Figure 1d. $(Si/Al)_2(O/N)$ is shown as corner-sharing tetrahedra with neighboring three O/N.

Table 1. Crystallographic Data of $Eu_{3.60}LiSi_{13.78}Al_{6.03}O_{6.82}N_{22.59}$

formula mass/g·mol^{-1}	1528.66
crystal system	trigonal
space group	$P3m1$ (no. 156)
cell parameters/Å	a = 12.12130(11) and c = 4.89283(5)
V/Å^3	622.57(1)
Z	1
crystal size/mm^3	0.09 × 0.01 × 0.01
temperature/K	293
crystal form	columnar
diffractometer	Bruker APEXII CCD area detector
radiation type	Mo Kα (λ = 0.71073 Å)
scan mode	ω scan
Abs correction	multiscan (SADABS)
μ/mm^{-1}	9.91
$2\theta_{max}$/deg	35.1
measured reflections	26 188
independent reflections	2019
observed reflections	2014
$R[F^2 > 2\sigma(F^2)]$, w$R(F^2)$	0.015, 0.037
$\Delta\rho_{max}$, $\Delta\rho_{min}$/e Å^{-3}	2.48, −0.9
S	1.12

To confirm the crystal structure model obtained from the single-crystal XRD data, TEM measurements were performed. In the HAADF-STEM image along the [001] directions, the bright dots forming a triangle correspond to Eu1, as shown in Figure 1e. A bright dot surrounded by Eu1 triangles corresponds to Eu2. Because of the substitutional disorder by the alternative occupation of Eu2 (Eu2A, Eu2B) or $(Si/Al)_2(O/N)$, the Eu2 is less bright than Eu1. In the electron diffraction pattern, no streak was observed in the [001] direction, coinciding with disordering of Eu2A, Eu2B, and $(Si,Al)_2(O,N)$. The SAED patterns from [001] and [100] zone axes can be well indexed on the basis of a hexagonal unit cell, with parameters a = 12.122 Å and c = 4.893 Å. The lattice fringes of 1.062 nm in the HRTEM image correspond to the (010) planes of the hexagonal structure. Eu atoms are directly observed via HAADF-STEM images in atomic scale along the [001] and [100] direction, which is consistent with the structure model. The brightest dots correspond to Eu sites. The dots indicating the Eu2A and Eu2B sites overlap with each other in the HAADF-STEM image, as the distance between Eu2A and Eu2B sites (0.62 Å) is smaller than the resolution of JEM-ARM200F in STEM mode (0.8 Å).

The $Eu_{3.60}LiSi_{13.78}Al_{6.03}O_{6.82}N_{22.59}$ crystal showed very weak luminescence at UV-excitation because the rare earth site is fully occupied by Eu, resulting in concentration quenching. Crystals with the same type of crystal structure were found in

DOI: 10.1021/acsami.9b09982
ACS Appl. Mater. Interfaces 2019, 11, 29047−29055

Table 2. Atomic Coordinates, Isotropic Atomic Displacement Parameters, and Occupancies of $Eu_{3.60}LiSi_{13.78}Al_{6.03}O_{6.82}N_{22.59}$

atom	x	y	z	U_{eq}/Å^2	occupancy
Eu1	0.55401(2)	0.10801(2)	0.32409(11)	0.01789(6)	1
Eu2A	0	0	0.8037(8)	0.0721(9)	0.458
Eu2B	0	0	0.6765(16)	0.0303(11)	0.1381
Li1	0.3333	0.6667	0.836(6)	0.011(3)	1
Si/Al1	0.58927(8)	0.91989(8)	0.8080(3)	0.00464(13)	1
Si/Al2	0.50713(13)	0.75357(7)	0.3187(6)	0.0082(2)	1
Si/Al3	0.75605(9)	0.00212(9)	0.2976(3)	0.00446(15)	1
Si/Al4	0.81994(6)	0.18006(6)	0.7877(3)	0.0056(2)	1
Si/Al5	0.6667	0.3333	0.8256(12)	0.0130(4)	1
Si/Al6A	0	0	0.1449(15)	0.0082(6)	0.4038
Si/Al6B	0	0	0.4569(14)	0.0082(6)	0.4038
O/N1	0.8541(3)	0.1459(3)	0.4566(10)	0.0146(8)	1
O/N2	0.6064(3)	0.9219(3)	0.4552(7)	0.0100(5)	1
O/N3	0.8378(4)	0.9189(2)	0.2965(14)	0.0135(8)	1
O/N4	0.3333	0.6667	0.3956(15)	0.0120(14)	1
O/N5	0.5370(5)	0.7685(2)	0.9431(11)	0.0104(8)	1
O/N6	0.4813(2)	0.9625(4)	0.8779(7)	0.0082(7)	1
O/N7	0.7279(3)	0.0367(3)	0.9655(7)	0.0138(6)	1
O/N8	0.6667	0.3333	0.161(2)	0.0218(18)	1
O/N9	0.7404(3)	0.2596(3)	0.7103(13)	0.0185(9)	1
O/N10	0	0	0.8037(8)	0.0721(9)	0.4039

samples made using Sr- and La-containing starting compositions. The $Sr_{3.43}Eu_{0.15}LiSi_{14.27}Al_{5.56}O_{6.32}N_{23.10}$ and $La_{3.19}Eu_{0.41}LiSi_{15.29}Al_{4.51}O_{2.12}N_{27.28}$ crystals were found from the powder product from compositions of Sr/Eu/Li/Al/Si = 1:0.05:4:6.5:6.5 and La/Eu/Li/Al/Si = 0.9:0.1:0.9:9:7, respectively. The crystallographic data, the atomic coordinates, and isotropic displacement parameters are shown in the Supporting Information (Tables S1−S3). These new-found materials are generalized as a sialon phase with the formula $A_{4-m}B_nC_{19+2m}X_{29+m}$ (A = Sr, La, Eu, Ce; B = Li; C = Si, Al; X = O, N; $0 \le m \le 1$; $0 \le n \le 1$), [$Eu_{3.60}LiSi_{13.78}Al_{6.03}O_{6.82}N_{22.59}$ (m = 0.40, n = 1), $Sr_{3.43}Eu_{0.15}LiSi_{14.27}Al_{5.56}O_{6.32}N_{23.10}$ (m = 0.41, n = 1), $La_{3.19}Eu_{0.41}LiSi_{15.29}Al_{4.51}O_{2.12}N_{27.28}$ (m = 0.40, n = 1)]. It can also be expressed as $A_3B_nC_{19}X_{29}(C_2X)_mA_{1-m}$ by extracting the disorder part. The site occupancy of the B site (Li) was fixed to 1 because the refined value was nearly 1. The x value corresponds to the ratio of A (Eu, Sr, La) and $(Si/Al)_2(O/N)$ at the substitutional disorder part on the (0, 0, z) axis. The similar x values in three crystals indicate that the new sialon phase is stable in some composition range. The $Sr_{3.43}Eu_{0.15}LiSi_{14.27}Al_{5.56}O_{6.32}N_{23.10}$ and $La_{3.19}Eu_{0.41}LiSi_{15.29}Al_{4.51}O_{2.12}N_{27.28}$ crystals showed cyan and blue luminescence under UV-excitation, as shown in Figure 2a,b, respectively. The emission spectra excited by 370 nm light are shown in the inset. To characterize the detailed luminescence properties of these new phosphors, powder syntheses of these phosphors were carried out.

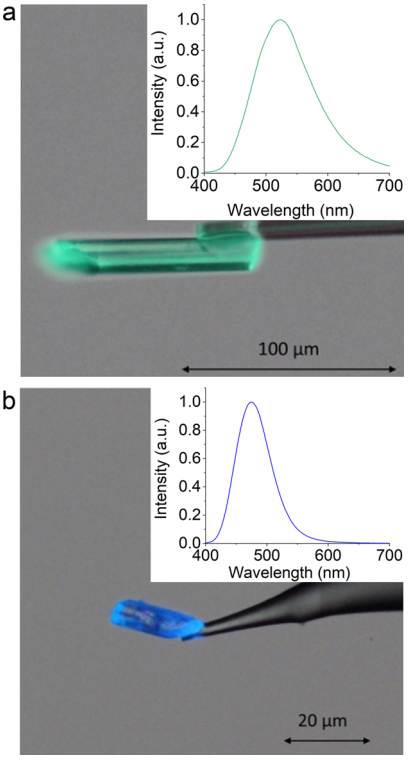

Figure 2. Luminescence photos and emission spectra of $Sr_{3.43}Eu_{0.15}LiSi_{14.27}Al_{5.56}O_{6.32}N_{23.10}$ (a) and $La_{3.19}Eu_{0.41}LiSi_{15.29}Al_{4.51}O_{2.12}N_{27.28}$ (b) single particles. The single particles were irradiated with a 370 nm LED.

3.2. Synthesis and Photoluminescence Properties of Eu-Doped Sr-Sialon and LaSr-Sialon Powder Phosphors. The powder samples were prepared according to the single-crystal compositions described in the previous section. A 1% Eu-doped Sr-sialon powder sample was made with the nominal chemical composition of $Sr_{3.57}Eu_{0.04}LiSi_{14.27}Al_{5.61}O_{6.19}N_{23.25}$ (Sr-sialon:0.01Eu). The sample is phase pure, which can be seen from the powder XRD patterns shown as the Supporting Information in Figure S1. The peak position and intensity almost coincided with those of the powder XRD pattern calculated from the crystallographic data obtained by the single-crystal XRD analysis. The synthesis of a phase pure 1% Eu-doped La-sialon, however, proved to be more difficult and it resulted in samples with low luminescence efficiency. In order to enhance the efficiency and obtain high phase purity, some of the La was substituted by Sr, leading to the nominal chemical composition of $La_{2.85}Sr_{0.72}Eu_{0.04}LiSi_{14.86}Al_{4.93}O_{2.89}$-

DOI: 10.1021/acsami.9b09982
ACS Appl. Mater. Interfaces 2019, 11, 29047−29055

$N_{26.51}$ (LaSr-sialon:0.01Eu), which can be seen in the Supporting Information Figure S1.

When excited at 355 nm, Sr-sialon:0.01Eu and LaSr-sialon:0.01Eu samples both emit blue light with a broad emission band centering at 475 and 470 nm, respectively (see Figure 3a, attributed to the Eu^{2+} 5d−4f transition. Note that

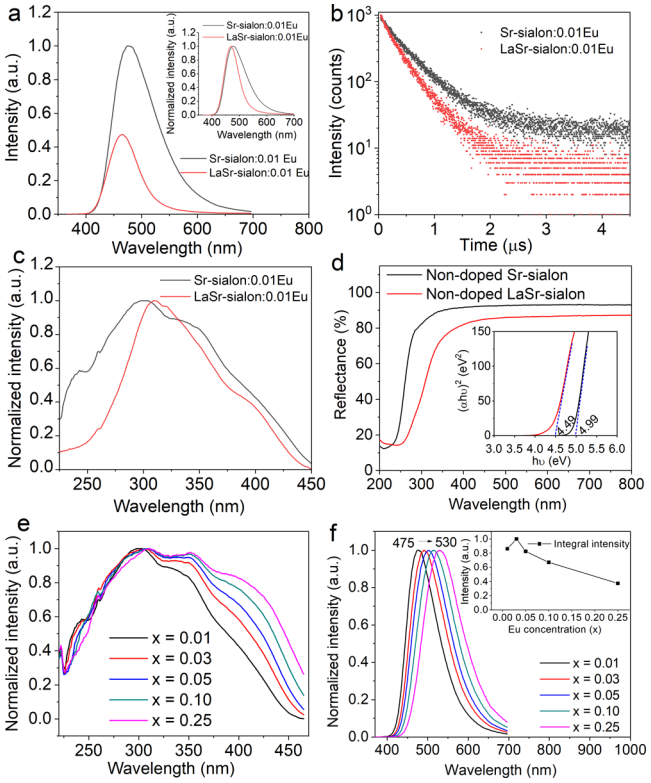

Figure 3. (a) Emission spectra, normalized emission spectra (inset) after 355 nm excitation, (b) luminescence decay curves after 370 nm nano-LED excitation, and (c) normalized excitation spectra by monitoring emission peak wavelength of 1% Eu-doped Sr-sialon and 1% Eu-doped LaSr-sialon powder phosphors; (d) diffuse reflectance spectra and the Kubelka−Munk absorption spectra (inset) for both $Sr_{3.61}LiSi_{14.27}Al_{5.61}O_{6.19}N_{23.25}$ (nondoped Sr-sialon) and $La_{2.85}Sr_{0.76}LiSi_{14.86}Al_{4.93}O_{2.89}N_{26.51}$ (nondoped LaSr-sialon) powder samples; (e) normalized excitation spectra and (f) normalized emission spectra and integral intensity (inset) of $Sr_{3.61(1-x)}Eu_{3.61x}LiSi_{14.27}Al_{5.61}O_{6.19}N_{23.25}$ (x = 0.01, 0.03, 0.05, 0.10 and 0.25) samples.

the emission wavelength in these powder phosphors is much shorter than that for the single particle discussed above ($Sr_{3.43}Eu_{0.15}LiSi_{14.27}Al_{5.56}O_{6.32}N_{23.10}$, around 530 nm). This is probably due to a higher Eu concentration in the single particle as compared to the powder phosphor. The Sr-sialon:0.01Eu phosphor displays a much broader emission band (fwhm = 90 nm) with higher luminescence intensity than that of the LaSr-sialon:0.01Eu phosphor (fwhm = 62 nm) because of more emission at the longer wavelength side (see inset of Figure 3a). Note that there are three Eu sites in the new sialon phase and the emission peak position is site-dependent. The higher emission at the longer wavelength side for Sr-sialon:0.01Eu, as compared to LaSr-sialon:0.01Eu, indicates that more Eu^{2+} ions occupy the lower energy site in Sr-sialon than in LaSr-sialon. The difference of emission colors in $Sr_{3.43}Eu_{0.15}LiSi_{14.27}Al_{5.56}O_{6.32}N_{23.10}$ and $La_{3.19}Eu_{0.41}LiSi_{15.29}Al_{4.51}O_{2.12}N_{27.28}$ single particles shown in Figure 2 can be explained in the same way. By further checking the luminescence decay for the powder samples (Figure 3b), one can see that the LaSr-sialon:0.01Eu sample shows faster decay than Sr-sialon:0.01Eu, which is consistent with the La-containing sample having a lower efficiency. Note also that, because of energy transfer, the longer-wavelength emission has longer decay time than the shorter-wavelength emission and that Sr-sialon:0.01Eu has a relatively larger contribution of longer-wavelength emission as compared to LaSr-sialon:0.01Eu.

In Figure 3c, the excitation spectra of Sr-sialon:0.01Eu and LaSr-sialon:0.01Eu are shown, monitoring the emission peak. Both spectra show a broad excitation band ranging from 200 to 450 nm, but the excitation spectrum of the LaSr-sialon:0.01Eu sample is much weaker than that of the Sr-sialon:0.01Eu sample at high energies (between 200 and 300 nm), see Figure 3c. This difference in strength of the excitation band can be explained by a difference in the band gap. In Figure 3d, the reflectance spectra of nondoped Sr-sialon ($Sr_{3.61}LiSi_{14.27}Al_{5.61}O_{6.19}N_{23.25}$) and nondoped LaSr-sialon ($La_{2.85}Sr_{0.76}LiSi_{14.86}Al_{4.93}O_{2.89}N_{26.51}$) are given, showing that the onset for the host-lattice absorption of the LaSr-sialon sample is at significantly longer wavelengths. The optical band gaps, as derived from the diffuse reflectance spectra,[32] for Sr-sialon and LaSr-sialon are estimated to be 4.99 and 4.49 eV, respectively (inset Figure 3c). As a result of the smaller band gap, LaSr-sialon:Eu has relatively more host-lattice absorption between 200 and 300 nm and, consequently, relatively less Eu^{2+} 4f−5d absorption in the 200−300 nm region than Sr-sialon:Eu. As 4f−5d absorption is generally much more efficient as compared to host lattice absorption in giving 5d−4f emission, the emission intensity of Sr-sialon:Eu is much higher than that of LaSr-sialon:Eu for excitation in the 250−300 nm range, explaining the difference in the excitation spectra.

In Figure 3e,f, the excitation and emission spectra of the new Sr-sialon phase doped with different Eu concentrations are shown. These samples were prepared with the nominal chemical composition of $Sr_{3.61(1-x)}Eu_{3.61x}LiSi_{14.27}Al_{5.61}O_{6.19}N_{23.25}$ (x = 0.01, 0.03, 0.05, 0.10 and 0.25). The position of the emission band maximum shifts from 475 nm at 1% Eu to 530 nm at 25% Eu, changing the emission from blue to green. A red shift is typically observed with increasing amount of Eu^{2+} as a result of a lowering of the 5d level in combination with reabsorption of emission light. In addition, the red shift of the emission with increasing Eu concentration may be enhanced for the new Sr-sialon phase because of the presence of Eu on different sites with different energies. With increasing Eu concentration, the energy transfer from the high-energy site to the low-energy site is enhanced, causing a red shift. The emission intensity of the new Sr-sialon phosphors initially increases with increasing Eu concentration because of higher absorption strength, reaching a maximum in luminescence intensity for a 3% Eu-doped sample. For higher Eu concentrations, the emission intensity starts to decrease as a result of concentration quenching. The excitation bands of the samples become broader with increasing Eu concentration, and the full width at half-maximum (fwhm) value for emission bands increases from 90 nm at 1% Eu to 110 nm at 25% Eu, which is typically observed for Eu^{2+}-doped samples. The highest IQE is equal to 55% for the 1% Eu-doped sample and the external quantum efficiency (IQE) reaches 37% for the 3% Eu-doped sample.

DOI: 10.1021/acsami.9b09982
ACS Appl. Mater. Interfaces 2019, 11, 29047−29055

3.3. Photoluminescence Properties of Ce-Doped $Sr_{3.61}LiSi_{14.27}Al_{5.61}O_{6.19}N_{23.25}$ and $La_{2.85}Sr_{0.76}LiSi_{14.86}Al_{4.93}O_{2.89}N_{26.51}$ Phosphors.

The phase pure Ce-doped $Sr_{3.61}LiSi_{14.27}Al_{5.61}O_{6.19}N_{23.25}$ and $La_{2.85}Sr_{0.76}LiSi_{14.86}Al_{4.93}O_{2.89}N_{26.51}$ phosphor powders were synthesized in a similar way as was done for the Eu-doped samples. The 1% Ce-doped $Sr_{3.61}LiSi_{14.27}Al_{5.61}O_{6.19}N_{23.25}$ (Sr-sialon) phosphor powder sample has a white body color. The excitation and emission spectra are shown in Figure 4a,b,

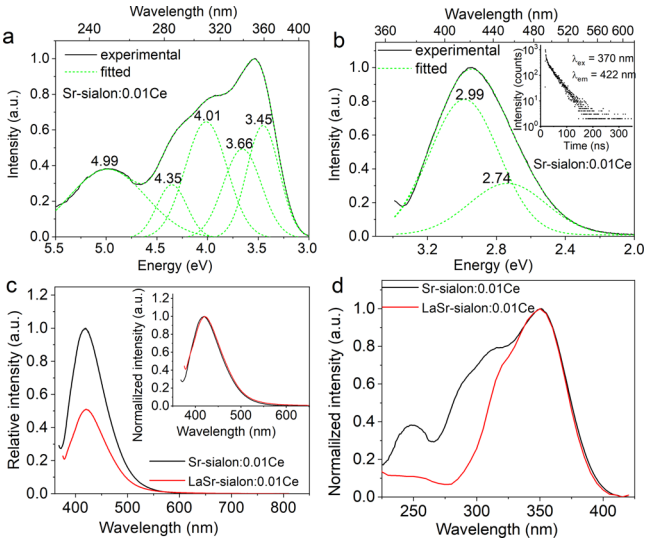

Figure 4. (a) Excitation spectrum monitoring 422 nm emission, (b) emission spectrum (λ_{ex} = 355 nm) and luminescence decay curve (inset) of 1% Ce doped $Sr_{3.61}LiSi_{14.27}Al_{5.61}O_{6.19}N_{23.25}$ (Sr-sialon:0.01Ce) phosphor; the comparison of emission spectra (c), excitation spectra (d), between Sr-sialon:0.01Ce and LaSr-sialon:0.01Ce ($La_{2.85}Sr_{0.76}LiSi_{14.86}Al_{4.93}O_{2.89}N_{26.51}$:0.01Ce) phosphors.

respectively. The excitation at 355 nm results in a deep-blue emission. The emission band centered at 422 nm (2.94 eV) is composed of two bands, centering at 2.99 eV (415 nm) and 2.74 eV (453 nm). These bands are assigned to the emission from the 5d excited state to the $^2F_{5/2}$ and $^2F_{7/2}$ ground states, respectively, because the energy difference of 0.25 eV is very close to the expected energy difference between the $^2F_{5/2}$ and $^2F_{7/2}$ states.[33] The excitation spectrum of 1% Ce-doped $Sr_{3.61}LiSi_{14.27}Al_{5.61}O_{6.19}N_{23.25}$ sample (see Figure 4a), monitoring the 422 nm emission, can be well fitted with five Gaussian curves, centering at 4.99, 4.35, 4.01, 3.66, and 3.45 eV. The energy band at 3.45 eV can be assigned to the lowest 4f−5d transition of Ce^{3+}, meaning that the $Sr_{3.61}LiSi_{14.27}Al_{5.61}O_{6.19}N_{23.25}$:0.01Ce phosphor has a Stokes shift of 0.46 eV. As the emission band can be well fitted with two Gaussian curves, it is suggested that the Ce emission mostly originates from one crystallographic site. This is confirmed by its single exponential decay behavior, as shown in the inset of Figure 4b.

After the 355 nm excitation, the La-containing sample displays a similar emission spectrum as that of the Sr-sialon sample without La, as the bandwidth and emission maximum are the same (Figure 4c). However, the luminescence intensity reduces by 48% for the La sample as compared to the Sr sample. When comparing the excitation spectra (monitoring the 422 nm emission) of a 1% Ce-doped $La_{2.85}Sr_{0.76}LiSi_{14.86}Al_{4.93}O_{2.89}N_{26.51}$ (LaSr-sialon:0.01Ce) sample with a 1% Ce-doped $Sr_{3.61}LiSi_{14.27}Al_{5.61}O_{6.19}N_{23.25}$ (Sr-sialon:0.01Ce) sample (Figure 4d), no difference in the excitation band maximum position is observed, and the normalized excitation spectra overlap between 330 and 400 nm. The similarities in the excitation and emission spectra indicate that there is no shift in the 4f−5d energy after introducing La to the structure. At higher energies, below 330 nm, the excitation spectrum of the LaSr-sialon:0.01Ce sample is much weaker than that of the Sr-sialon:0.01Ce sample. The difference in intensity below 330 nm can be understood considering the smaller band gap of LaSr-sialon as compared to that of Sr-sialon, similar to what was discussed before for the Eu-doped Sr-sialon and LaSr-sialon samples.

The samples with different Ce concentrations were prepared for the following compositions: $Sr_{3.61(1-y)}Ce_{3.61y}LiSi_{14.27}Al_{5.61}O_{6.19}N_{23.25+1.203y}$ (y = 0.01, 0.03, 0.05, 0.10, 0.25). The XRD patterns (Supporting Information Figure S2) indicate that, up to a Ce concentration of 10%, the samples are phase pure. For the 25% Ce-containing sample a small amount of unknown impurity is detected. With increasing Ce concentration, the position of the Ce^{3+} 5d−4f emission band in the Ce-doped new Sr-sialon phase phosphors shifts from 422 nm for 1% Ce to 441 nm for the 25% Ce-doped sample, as shown in Figure 5a. The red shift of the emission can be explained by

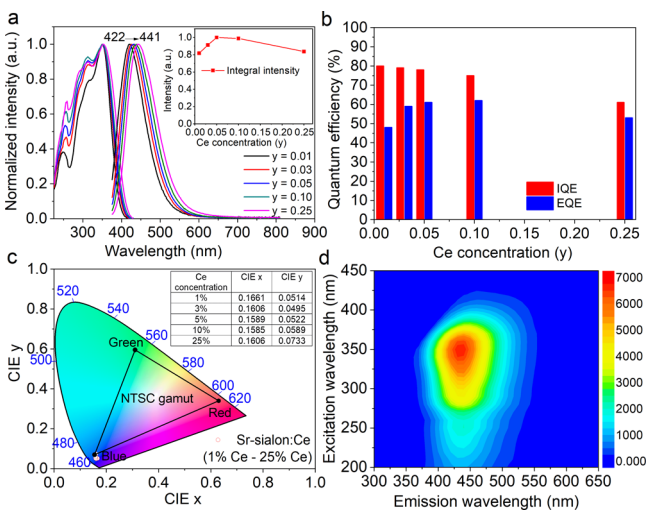

Figure 5. (a) Normalized excitation (monitoring the emission maxima) and emission spectra (excited at 355 nm) of the Sr-sialon:Ce phosphors for different Ce concentrations, the emission intensity is shown in the inset; (b) IQE and EQE of the Sr-sialon:Ce phosphors as a function of the Ce concentration; (c) CIE chromaticity diagram indicating the color coordinates of the Sr-sialon:Ce phosphors for different Ce concentrations; (d) 2D photoluminescence spectrum showing the dependence of the emission intensity on the excitation wavelength for Sr-sialon:5% Ce.

reabsorption and energy transfer.[30] The highest IQE of 80% is obtained for the 1% Ce-doped sample (Figure 5b). When the Ce concentration is increased to 5 and 10%, the IQE value only reduces to 78 and 75%, respectively, indicating a very small concentration quenching. The EQE is highest for the 10% Ce-doped sample with the efficiency of 62%. It is noted that Ce-doped $Sr_{3.61(1-y)}LiSi_{14.27}Al_{5.61}O_{6.19}N_{23.25+1.203y}$ phosphors have still a relatively high IQE and EQE at high dopant concentrations.

As mentioned before, the Ce emission mostly originates from Ce at only one crystallographic site. This emission probably is from Ce at the Sr1 site. This assumption is based

DOI: 10.1021/acsami.9b09982
ACS Appl. Mater. Interfaces 2019, 11, 29047−29055

on the shift of the emission band when increasing the Ce doping concentration from 1 to 25%. This shift is continuous without significant broadening of the emission band, implying that the relative distribution of Ce over the sites remains similar. From the single-crystal XRD result of $Sr_{3.43}Eu_{0.15}LiSi_{14.27}Al_{5.56}O_{6.32}N_{23.10}$, the Sr/Eu1−Sr/Eu2−Sr/Eu3 ratio is 3.0:0.49:0.1. As the Ce amount in the 25% Ce-doped sample (3.59 × 0.25 = 0.90) largely exceeds the sum of Sr/Eu2 and Sr/Eu3 (0.49 + 0.1 = 0.59), a high Ce concentration at only one site is only possible if that site is the Sr1 site.

With increasing Ce concentration, the CIE coordinates shift from (0.166, 0.051) for 1% Ce to (0.161, 0.073) for 25% Ce (Figure 5c). For 5% Ce doping, the CIE coordinates are x = 0.159 and y = 0.052. Note that for all samples the CIE coordinates are very close to the NTSC blue standard (0.155, 0.070), signifying a high color purity. As shown by the 2D photoluminescence spectrum in Figure 5d, the deep-blue emission of the 5% Ce-doped Sr-sialon sample displays high color stability under various excitation wavelengths (200−400 nm), as almost no shift of the emission peak can be observed.

3.4. Thermal Quenching of the Luminescence of Ce- and Eu-Doped Sr-Sialon and LaSr-Sialon. In order to understand the difference of luminescence intensity at 355 nm excitation between Eu- and Ce-doped LaSr-sialon and Sr-sialon phosphors, the temperature-dependent emission was investigated between 4 and 573 K. For the Sr-sialon:0.01Ce sample, the luminescence intensity remains almost constant between 4 and 200 K and only 8% of the luminescence is quenched at room temperature compared to the intensity at 4 K (see Figure 6). However, the La-containing sample already starts to quench at above 100 K, reducing the intensity by 32% at room temperature. As the La-containing sample is more thermally quenched at 300 K, it is less efficient than the sample without La at room temperature. Above 200 K, a nearly linear decrease of intensity with increasing temperature can be observed for the La-containing sample, and only 28% of the luminescence is left at 573 K. For the 1% Ce-doped Sr-sialon sample, the luminescence intensity decreases slowly with increasing temperature and there is still 78% left at 473 K and 69% left at 573 K. Its good stability against thermal quenching is an advantage for application in a high-power white LED. Note that for both Sr-sialon:0.01Ce and LaSr-sialon:0.01Ce the shape and position of the emission peak do not shift at all between 4 and 573 K (see Figure S3), which is a further indication that the Ce emission is all from Ce at only one distinct crystallographic site, as discussed before. By cooling down the phosphors back to room temperature, the luminescence intensity is almost fully restored, indicating that the phosphors have good thermal stability.

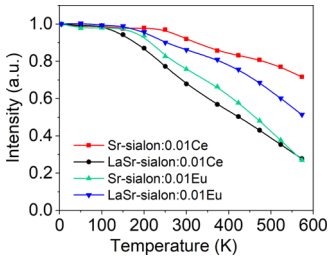

Figure 6. Temperature dependency of the luminescence intensity of 1% Ce-doped Sr-sialon, 1% Ce-doped LaSr-sialon, 1% Eu-doped Sr-sialon, and 1% Eu-doped LaSr-sialon phosphors.

Compared to Ce-doped samples, the luminescence of 1% Eu-doped Sr-sialon starts to quench at above 150 K (Figure 6). At room temperature, about 25% of the emission intensity has been quenched and, at 573 K the emission intensity has decreased to 27% compared to the original intensity at 4 K. Together with the intensity decrease with increasing temperature, a blue shift of the emission is observed with the maximum shifting from 477 nm at 4 K to 466 nm at 573 K. As compared to Sr-sialon:0.01Eu, LaSr-sialon:0.01Eu quenches much slower. For the LaSr-sialon:0.01Eu sample, only 14% of the luminescence is quenched at room temperature and 51% left at 573 K, compared to the intensity at 4 K. As mentioned above, the LaSr-sialon:0.01Eu has a relatively smaller contribution of emission from Eu at the low energy site (see inset Figure 3a). This difference may give an explanation for the faster thermal quenching of Sr-sialon:0.01Eu as compared to LaSr-sialon:Eu, if the Eu at the low energy site quenches faster than Eu at the high-energy site.

There is an interesting difference when comparing the thermal quenching behaviors of the Eu- and Ce-doped Sr-sialon and LaSr-sialon samples. In the Sr-sialon samples, the Eu emission quenches faster than the Ce emission, whereas in the LaSr-sialon samples, the opposite trend is observed as the Ce emission quenches faster than the Eu emission. In most other phosphors, the quenching of the Eu emission is faster than the quenching of the Ce emission, because the quenching is often caused by thermal ionization[34] of an electron from the 5d level to the conduction band and the lowest 5d level of Eu^{2+} is closer to the conduction band than the lowest 5d level of Ce^{3+}. The faster thermal quenching of the Ce emission in LaSr-sialon, therefore, suggests that other factors play a role in the emission quenching. It may, for example, be related to energy transfer and quenching at defects, considering the disorder in the structure of this phosphor, as well as the presence of multiple crystallographically different sites at which Ce and Eu can substitute.

3.5. Application of the $Sr_{3.61}LiSi_{14.27}Al_{5.61}O_{6.19}N_{23.25}$:0.05Ce Phosphor in a White LED. A white LED has been fabricated with 5% Ce-doped Sr-sialon phosphor as the blue component, in combination with a 365 nm UV LED chip, a green-emitting $SrSi_2O_2N_2:Eu^{2+}$ phosphor (emission maximum at 540 nm, EQE = 75%), and a red-emitting $Sr_{0.9}Ca_{0.1}AlSiN_3:Eu^{2+}$ phosphor (emission maximum at 620 nm, EQE = 76%). The emission spectra of all phosphor components are shown in the Supporting Information (Figure S4). One can see from Figure 7a that the fabricated white LED has excellent color-rendering indices (see Table 3) with R_a = 96 and R_{12} = 97 at a flux current of 20 mA. The white LED has a correlated color temperature (CCT) of 4255 K and chromaticity coordinates of x = 0.366 and y = 0.353, giving a bright natural white light. A luminous efficacy of 17.8 lm/W has been obtained for this white LED device. These performances make Ce-doped $Sr_{3.61}LiSi_{14.27}Al_{5.61}O_{6.19}N_{23.25}$ a promising blue phosphor for illumination grade white LEDs.

Recently, we reported[5] another highly efficient deep-blue-emitting Ce-doped La N-phase ($La_3Si_{6.5}Al_{1.5}O_{5.5}N_{9.5}$:Ce) phosphor as a component of a warm white LED with a high color-rendering index. In comparison to this phosphor, the Ce-doped $Sr_{3.61}LiSi_{14.27}Al_{5.61}O_{6.19}N_{23.25}$ phosphor designed in the present contribution is more thermally stable. At around 200 °C, the photoluminescence intensity of $Sr_{3.61}LiSi_{14.27}Al_{5.61}$-

DOI: 10.1021/acsami.9b09982
ACS Appl. Mater. Interfaces 2019, 11, 29047−29055

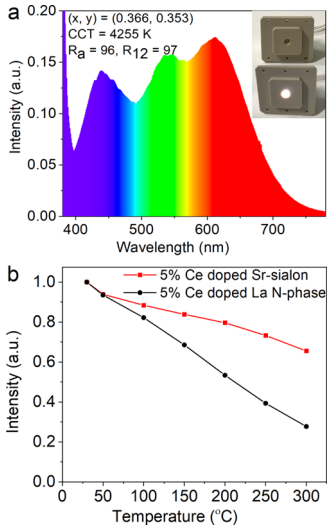

Figure 7. (a) Electroluminescence spectrum of a white LED using a 5% Ce-doped $Sr_{3.61}LiSi_{14.27}Al_{5.61}O_{6.19}N_{23.25}$ as a blue phosphor component, in which a 365 nm UVLED chip and a green-emitting $SrSi_2O_2N_2:Eu^{2+}$ phosphor and a red-emitting $Sr_{0.9}Ca_{0.1}AlSiN_3:Eu^{2+}$ phosphor were used. The photographs of the LED in off and on states are shown in the inset. (b) Comparison of temperature dependences of emission intensity (30−300 °C) obtained for 5% Ce-doped $Sr_{3.61}LiSi_{14.27}Al_{5.61}O_{6.19}N_{23.25}$ (Sr-sialon) and La N-phase ($La_3Si_{6.5}Al_{1.5}O_{5.5}N_{9.5}$:Ce) phosphors.

$O_{6.19}N_{23.25}$ is still at 80%, as compared to the intensity at 30 °C, whereas there is only 53% left for the $La_3Si_{6.5}Al_{1.5}O_{5.5}N_{9.5}$:Ce phosphor at 200 °C (Figure 7b). The large difference may be explained by the difference in band gap: the band gap of the Sr-sialon phase (4.99 eV) is much larger than that of $La_3Si_{6.5}Al_{1.5}O_{5.5}N_{9.5}$:Ce (4.34 eV). This probably shifts the lowest 5d level further away from the bottom of the conduction band in $Sr_{3.61}LiSi_{14.27}Al_{5.61}O_{6.19}N_{23.25}$, resulting in a higher activation energy for thermal quenching.

4. CONCLUSIONS

The newly discovered sialon $A_{4-m}B_nC_{19+2m}X_{29+m}$ (A = Sr, La, Eu, Ce; B = Li; C = Si, Al; X = O, N; $0 \le m \le 1$; $0 \le n \le 1$) crystallizes in a trigonal unit cell with the *P*3*m*1 space group (no. 156). The structure is characterized by two crystallographically different A (A = Sr, Eu, La) cation sites, of which the A2 site has both a positional disorder (A2a/A2b) as well as a substitutional disorder with $(Si/Al)_2(O/N)$. Both the $Sr_{3.61}LiSi_{14.27}Al_{5.61}O_{6.19}N_{23.25}$ (Sr-sialon) and the $La_{2.85}Sr_{0.76}LiSi_{14.86}Al_{4.93}O_{2.89}N_{26.51}$ (LaSr-sialon) hosts can be doped with either Eu^{2+} or Ce^{3+}. Doping with 1% Eu^{2+} results in a broad emission band centered at 475 nm for Sr-sialon and 470 nm for LaSr-sialon. An IQE up to 55% has been reached for Sr-sialon:Eu, whereas the LaSr-sialon:Eu is less efficient. On the other hand, the quenching of the Sr-sialon:Eu phosphor is significantly faster than that of the LaSr-sialon:Eu phosphor. The 1% Ce-doped Sr-sialon shows a deep-blue emission (λ_{em} = 422 nm, fwhm = 80 nm) after the 355 nm excitation with an IQE of 80%. Ce-doped LaSr-sialon gives a similar emission, but with lower efficiency and faster thermal quenching, because of the reduction of the band gap after La substitution. Compared to other highly efficient deep-blue-emitting (oxy-)nitride phosphors, the newly reported Sr-sialon:Ce phosphor has a much better stability against thermal quenching, retaining a relative intensity of 80% at 200 °C as compared to the intensity at room temperature. Moreover, the shape and the position of the emission band do not change with temperature, indicating excellent color stability. The newly reported Ce-doped Sr-sialon phosphor shows the highest luminescence intensity at a Ce dopant concentration of 10%. At higher Ce contents, the concentration quenching comes into effect, although the reduction of the EQE at high Ce concentrations is relatively minor as compared to that in other Ce-doped phosphors. In addition, a white LED made using the newly reported Sr-sialon:Ce phosphor as the blue phosphor component shows excellent color-rendering indices (R_a = 96 and R_{12} = 97) with a CCT of 4255 K and chromaticity coordinates of x = 0.366 and y = 0.353. These performances indicate that the newly reported Ce-doped Sr-sialon phase is a highly promising deep-blue phosphor for high-color-rendering warm white LEDs.

■ ASSOCIATED CONTENT

Supporting Information

The Supporting Information is available free of charge on the ACS Publications website at DOI: 10.1021/acsami.9b09982.

Crystallographic data for $Eu_{3.60}LiSi_{13.78}Al_{6.03}O_{6.82}N_{22.59}$ (CIF)

Crystallographic data for $Sr_{3.43}Eu_{0.15}LiSi_{14.27}Al_{5.56}O_{6.32}N_{23.10}$ (CIF)

Crystallographic data for $La_{3.19}Eu_{0.41}LiSi_{15.29}Al_{4.51}O_{2.12}N_{27.28}$ (CIF)

Atomic coordinates, isotropic atomic displacement parameters, and occupancies of $Sr_{3.43}Eu_{0.15}LiSi_{14.27}Al_{5.56}O_{6.32}N_{23.10}$ and $La_{3.19}Eu_{0.41}LiSi_{15.29}Al_{4.51}O_{2.12}N_{27.28}$ single particles; XRD patterns, temperature dependency emission spectra of Eu-doped and Ce-doped La-sialon, LaSr-sialon, and Sr-sialon powder samples; and emission spectra of phosphors used for a white LED fabrication (PDF)

■ AUTHOR INFORMATION

Corresponding Authors

*E-mail: wangcy0317@gmail.com (C.-Y.W.).

*E-mail: takeda.takashi@nims.go.jp (T.T.).

ORCID

Chun-Yun Wang: 0000-0002-1320-1296

Notes

The authors declare no competing financial interest.

■ ACKNOWLEDGMENTS

This work was supported by JSPS KAKENHI (JP26420691) and the National Nature Science Foundation of China (no. 51832005). We would like to acknowledge Kazuko Nakajima for the quantum efficiency measurement, and Yoshihiro Nemoto and Akira Hasegawa for TEM measurement.

Table 3. Color Rendering Indices of the White LED Containing 5% Ce-Doped Sr-Sialon Deep-Blue-Emitting Phosphor

R_a	R_1	R_2	R_3	R_4	R_5	R_6	R_7	R_8	R_9	R_{10}	R_{11}	R_{12}	R_{13}	R_{14}	R_{15}
96	99	98	96	96	99	97	95	92	80	95	96	97	98	97	97

DOI: 10.1021/acsami.9b09982
ACS Appl. Mater. Interfaces 2019, 11, 29047−29055

REFERENCES

(1) Izhevskiy, V. A.; Gênova, L. A.; Bressiani, J. C. Review Article: RE-SiAlON α/ β-composites. Formation, Thermal Stability, Phase Relationships, Reaction Densification. *Cerâmica* **1999**, *45*, 05−23.

(2) Cao, G. Z.; Metselaar, R. .alpha.'-Sialon ceramics: a review. *Chem. Mater.* **1991**, *3*, 242−252.

(3) Hirosaki, N.; Xie, R.-J.; Kimoto, K.; Sekiguchi, T.; Yamamoto, Y.; Suehiro, T.; Mitomo, M. Characterization and Properties of Green-emitting β-SiAlON:Eu^{2+} Powder Phosphors for White Light-emitting Diodes. *Appl. Phys. Lett.* **2005**, *86*, 211905.

(4) Xie, R.-J.; Hirosaki, N.; Mitomo, M.; Yamamoto, Y.; Suehiro, T.; Ohashi, N. Photoluminescence of Cerium-Doped α-SiAlON Materials. *J. Am. Ceram. Soc.* **2004**, *87*, 1368−1370.

(5) Wang, C.-Y.; Takeda, T.; Ten Kate, O. M.; Tansho, M.; Deguchi, K.; Takahashi, K.; Xie, R.-J.; Shimizu, T.; Hirosaki, N. Ce-Doped $La_3Si_{6.5}Al_{1.5}N_{9.5}O_{5.5}$, a Rare Highly Efficient Blue-Emitting Phosphor at Short Wavelength toward High Color Rendering White LED Application. *ACS Appl. Mater. Interfaces* **2017**, *9*, 22665−22675.

(6) Oeckler, O.; Kechele, J. A.; Koss, H.; Schmidt, P. J.; Schnick, W. $Sr_5Al_{5+x}Si_{21-x}N_{35-x}O_{2+x}$:$Eu^{2+}$ (x≈0) − A Novel Green Phosphor for White-light pcLEDs with Disordered Intergrowth Structure. *Chem.—Eur. J.* **2009**, *15*, 5311−5319.

(7) Li, Y. Q.; de With, G.; Hintzen, H. T. Luminescence Properties of Eu^{2+}-Doped $MAl_{2-x}Si_xO_{4-x}N_x$ (M = Ca, Sr, Ba) Conversion Phosphor for White LED Applications. *J. Electrochem. Soc.* **2006**, *153*, G278−G282.

(8) Park, W. B.; Singh, S. P.; Kim, M.; Sohn, K.-S. Combinatorial Screening of Luminescent and Structural Properties in a Ce^{3+}-doped Ln-Al-Si-O-N (Ln = Y, La, Gd, Lu) System: the Discovery of a Novel $Gd_3Al_{3+x}Si_{3-x}O_{12+x}N_{2-x}$:$Ce^{3+}$ Phosphor. *Inorg. Chem.* **2015**, *54*, 1829−1840.

(9) Tang, J.-Y.; Xie, W.-J.; Huang, K.; Hao, L.-Y.; Xu, X.; Xie, R.-J. A high Stable Blue $BaSi_3Al_3O_4N_5$:Eu^{2+} Phosphor for White LEDs and Display Applications. *Electrochem. Solid-State Lett.* **2011**, *14*, J45−J47.

(10) Wang, C.-Y.; Kate, O. M. t.; Takeda, T.; Hirosaki, N. Efficient and Thermally Stable Blue-emitting Ce^{3+} doped $LaAl(Si_{6-z}Al_z)(N_{10-z}O_z)$ (JEM:Ce) Phosphors for White LEDs. *J. Mater. Chem. C* **2017**, *5*, 8295−8300.

(11) George, N. C.; Denault, K. A.; Seshadri, R. Phosphors for Solid-State White Lighting. *Annu. Rev. Mater. Res.* **2013**, *43*, 481−501.

(12) McKittrick, J.; Hannah, M. E.; Piquette, A.; Han, J. K.; Choi, J. I.; Anc, M.; Galvez, M.; Lugauer, H.; Talbot, J. B.; Mishra, K. C. Phosphor Selection Considerations for Near-UV LED Solid State Lighting. *ECS J. Solid State Sci. Technol.* **2013**, *2*, R3119−R3131.

(13) Wang, L.; Wang, X.; Takeda, T.; Hirosaki, N.; Tsai, Y.-T.; Liu, R.-S.; Xie, R.-J. Structure, Luminescence, and Application of a Robust Carbidonitride Blue Phosphor ($Al_{1-x}Si_xC_xN_{1-x}$:Eu^{2+}) for Near UV-LED Driven Solid State Lighting. *Chem. Mater.* **2015**, *27*, 8457−8466.

(14) Piquette, A.; Bergbauer, W.; Galler, B.; Mishra, K. C. On Choosing Phosphors for Near-UV and Blue LEDs for White Light. *ECS J. Solid State Sci. Technol.* **2016**, *5*, R3146−R3159.

(15) Dierre, B.; Xie, R.-J.; Hirosaki, N.; Sekiguchi, T. Blue Emission of Ce^{3+} in Lanthanide Silicon Oxynitride Phosphors. *J. Mater. Res.* **2007**, *22*, 1933−1941.

(16) LU, F.; Lijing, B.; Zhiping, Y.; Quanlin, L. Photoluminescence Properties of Ce^{3+} doped $YSiO_2N$ Blue-emitting Phosphors. *J. Rare Earths* **2012**, *30*, 851−855.

(17) Zhang, Z.-J.; Cho, H. Y.; Yang, W. Preparation and Luminescence Properties of Ce^{3+}-doped $Gd_5Si_3O_{12}N$ Phosphor Emerging Red Shift. *Mater. Res. Bull.* **2017**, *88*, 330−336.

(18) Suehiro, T.; Hirosaki, N.; Xie, R.-J.; Sato, T. Blue-emitting $LaSi_3N_5$:Ce^{3+} Fine Powder Phosphor for UV-converting White Light-emitting Diodes. *Appl. Phys. Lett.* **2009**, *95*, 051903.

(19) Inoue, K.; Hirosaki, N.; Xie, R.-J.; Takeda, T. Highly Efficient and Thermally Stable Blue-emitting AlN:Eu^{2+} Phosphor for Ultraviolet White Light-emitting Diodes. *J. Phys. Chem. C* **2009**, *113*, 9392−9397.

(20) Wang, L.; Xie, R.-J.; Suehiro, T.; Takeda, T.; Hirosaki, N. Down-Conversion Nitride Materials for Solid State Lighting: Recent Advances and Perspectives. *Chem. Rev.* **2018**, *118*, 1951−2009.

(21) Xia, Z.; Xu, Z.; Chen, M.; Liu, Q. Recent Developments in the New Inorganic Solid-State LED Phosphors. *Dalton Trans.* **2016**, *45*, 11214−11232.

(22) Park, W. B.; Shin, N.; Hong, K.-P.; Pyo, M.; Sohn, K.-S. A New Paradigm for Materials Discovery: Heuristics-Assisted Combinatorial Chemistry Involving Parameterization of Material Novelty. *Adv. Funct. Mater.* **2012**, *22*, 2258−2266.

(23) Hirosaki, N.; Takeda, T.; Funahashi, S.; Xie, R.-J. Discovery of New Nitridosilicate Phosphors for Solid State Lighting by the Single-Particle-Diagnosis Approach. *Chem. Mater.* **2014**, *26*, 4280−4288.

(24) Takeda, T.; Hirosaki, N.; Funahashi, S.; Xie, R.-J. New Phosphor Discovery by the Single Particle Diagnosis Approach. *Mater. Discov.* **2015**, *1*, 29−37.

(25) ten Kate, O. M.; Xie, R.-J.; Wang, C.-Y.; Funahashi, S.; Hirosaki, N. Eu^{2+}-Doped $Sr_2B_{2-2x}Si_{2+3x}Al_{2-x}N_{8+x}$: A Boron-Containing Orange-Emitting Nitridosilicate with Interesting Composition-Dependent Photoluminescence Properties. *Inorg. Chem.* **2016**, *55*, 11331−11336.

(26) Takeda, T.; Hirosaki, N.; Funahshi, S.; Xie, R.-J. Narrow-Band Green-Emitting Phosphor $Ba_2LiSi_7AlN_{12}$:Eu^{2+} with High Thermal Stability Discovered by a Single Particle Diagnosis Approach. *Chem. Mater.* **2015**, *27*, 5892−5898.

(27) Wang, X.-J.; Wang, L.; Takeda, T.; Funahashi, S.; Suehiro, T.; Hirosaki, N.; Xie, R.-J. Blue-Emitting $Sr_3Si_{8-x}Al_xO_{7+x}N_{8-x}$:$Eu^{2+}$ Discovered by a Single-Particle-Diagnosis Approach: Crystal Structure, Luminescence, Scale-Up Synthesis, and Its Abnormal Thermal Quenching Behavior. *Chem. Mater.* **2015**, *27*, 7689−7697.

(28) Sheldrick, G. *SADABS, Multi-Scan Absorption Correction*, Version 2; Bruker AXS Inc.: Madison, WI, 2012.

(29) Sheldrick, G. M. A short history of SHELX. *Acta Crystallogr., Sect. A: Found. Crystallogr.* **2008**, *64*, 112−122.

(30) Wang, C.-Y.; Takeda, T.; ten Kate, O. M.; Xie, R.-J.; Takahashi, K.; Hirosaki, N. Synthesis and Photoluminescence Properties of a Phase Pure Green-emitting Eu doped JEM sialon ($La-Si_{6-z}Al_{1+z}N_{10-z}O_z$, z∼1) Phosphor with a Large Red-shift of Emission and Unusual Thermal Quenching Behavior. *J. Mater. Chem. C* **2016**, *4*, 10358−10366.

(31) Momma, K.; Izumi, F. VESTA 3 for Three-dimensional Visualization of Crystal, Volumetric and Morphology Data. *J. Appl. Crystallogr.* **2011**, *44*, 1272−1276.

(32) Suehiro, T.; Tansho, M.; Shimizu, T. Na-α'-GeGaON Solid Solution Analogous to α'-SiAlON: Synthesis, Crystal Structure, and Potentiality as a Photocatalyst. *Inorg. Chem.* **2016**, *55*, 2355−2362.

(33) Smet, P. F.; Parmentier, A. B.; Poelman, D. Selecting Conversion Phosphors for White Light-emitting Diodes. *J. Electrochem. Soc.* **2011**, *158*, R37−R54.

(34) Kamada, K.; Endo, T.; Tsutumi, K.; Yanagida, T.; Fujimoto, Y.; Fukabori, A.; Yoshikawa, A.; Pejchal, J.; Nikl, M. Composition Engineering in Cerium-Doped $(Lu,Gd)_3(Ga,Al)_5O_{12}$ Single-Crystal Scintillators. *Cryst. Growth Des.* **2011**, *11*, 4484−4490.

DOI: 10.1021/acsami.9b09982
ACS Appl. Mater. Interfaces 2019, 11, 29047−29055